Lithos 246–247 (2016) 48–60

Contents lists available at ScienceDirect

Lithos

journal homepage: www.elsevier.com/locate/lithos

Melt extraction and mantle source at a Southwest Indian Ridge Dragon Bone amagmatic segment on the Marion Rise

Changgui Gao [a,b], Henry J.B. Dick [b], Yang Liu [a], Huaiyang Zhou [a]

[a] State Key Lab of Marine Geology, Tongji University, Shanghai 20092, China
[b] Department of Geology and Geophysics, Woods Hole Oceanographic Institution, Woods Hole, MA 02543, USA

ARTICLE INFO

Article history:
Received 24 July 2015
Accepted 21 December 2015
Available online 12 January 2016

Keywords:
Abyssal peridotite
Mid-ocean ridge basalt
Previous melting
Buoyant upper mantle
Marion Rise
The Dragon Bone amagmatic segment

ABSTRACT

This paper works on the trace and major element compositions of spatially associated basalts and peridotites from the Dragon Bone amagmatic ridge segment at the eastern flank of the Marion Platform on the ultraslow spreading Southwest Indian Ridge. The rare earth element compositions of basalts do not match the pre-alteration Dragon Bone peridotite compositions, but can be modeled by about 5 to 10% non-modal batch equilibrium melting from a DMM source. The Dragon Bone peridotites are clinopyroxene-poor harzburgite with average spinel Cr# ~ 27.7. The spinel Cr# indicates a moderate degree of melting. However, CaO and Al_2O_3 of the peridotites are lower than other abyssal peridotites at the same Mg# and extent of melting. This requires a pyroxene-poor initial mantle source composition compared to either hypothetical primitive upper mantle or depleted MORB mantle sources. We suggest a hydrous melting of the initial Dragon Bone mantle source, as wet melting depletes pyroxene faster than dry. According to the rare earth element patterns, the Dragon Bone peridotites are divided into two groups. Heavy REE in Group 1 are extremely fractionated from middle REE, which can be modeled by ~7% fractional melting in the garnet stability field and another ~12.5 to 13.5% in the spinel stability field from depleted and primitive upper mantle sources, respectively. Heavy REE in Group 2 are slightly fractionated from middle REE, which can be modeled by ~15 to 20% fractional melting in the spinel stability field from a depleted mantle source. Both groups show similar melting degree to other abyssal peridotites. If all the melt extraction occurred at the middle oceanic ridge where the peridotites were dredged, a normal ~6 km thick oceanic crust is expected at the Dragon Bone segment. However, the Dragon Bone peridotites are exposed in an amagmatic ridge segment where only scattered pillow basalts lie on a partially serpentinized mantle pavement. Thus their depletion requires an earlier melting occurred at other place. Considering the hydrous melting of the initial Dragon Bone mantle source, we suggest the earlier melting event occurred in an arc terrain, prior to or during the closure of the Mozambique Ocean in the Neproterozoic, and the subsequent assembly of Gondwana. Then, the Al_2O_3 depleted and thus buoyant peridotites became the MORB source for Southwest Indian Ridge and formed the Marion Rise during the Gondwana breakup.

1. Introduction

Abyssal peridotites and mid-ocean ridge basalts (MORB) are considered complementary products of mantle melting and melt extraction that creates the ocean crust (Alard et al., 2005; Dick et al., 1984; Handler et al., 2005; Roy-Barman and Allègre, 1994; Snow and Reisberg, 1995). If the mantle source beneath the mid-ocean ridges was homogeneous, the abyssal peridotites show complementary variations, in terms of their mineralogy and chemistry, with the chemistry of spatially associated MORB (Dick and Natland, 1996; Johnson et al., 1990; Kelemen et al., 1997; Niu, 1997; Snow et al., 1994). These coherent features of abyssal peridotites and MORB suggest at least some of the melting is very recent. Then, it is reasonable to use $Na_{8.0}$ and $Fe_{8.0}$ ($Na_{8.0}$ and $Fe_{8.0}$ were calculated from the reported analyses after correction to 8.5 wt.% MgO by removal of Fo_{90} olivine. $Na_{8.0} = Na_2O + 0.373 * MgO - 2.98$. $Fe_{8.0} = FeO + 1.664 * MgO - 13.313$.) in MORB melts to infer the extent of mantle melting and thickness of oceanic crust (Klein and Langmuir, 1987). However, it is increasingly clear that the upper mantle is heterogeneous with pyroxenite or eclogite layers in all parameters at all scales (Dick et al., 1984; Niu et al., 2002; Salters and Dick, 2002; Seyler et al., 2003; Stracke, 2012). The preferential melting of pyroxenite and eclogite will mess up to estimate the thickness of oceanic crust. Moreover, remelting a previously depleted source would also yield low melt volumes, low sodium basalts, highly incompatible element depleted peridotites, and thin crust (Dick and Zhou, 2015; Dick et al., 1984; Niu, 2004). In the last two decades, Re–Os isotopic studies have indicated that some abyssal peridotites may have experienced multiple ancient melt extraction episodes (Alard et al., 2005; Brandon et al., 2000; Harvey et al., 2006; Ishikawa et al., 2011; Lassiter et al., 2014; Liu et al., 2008;

E-mail address: gaocg1214@gmail.com (C. Gao).

http://dx.doi.org/10.1016/j.lithos.2015.12.007
0024-4937/

Roy-Barman and Allègre, 1994), and some trace element variations in MORB can only explained by a previously depleted source (Hofmann, 1997). However, where this ancient melting occurred is generally not explained.

Here, we report whole-rock major and trace element compositions of abyssal peridotites, and spatially associated basalts from the Dragon Bone amagmatic segment of the Southwest Indian Ridge (SWIR). The extremely fractionated heavy rare earth elements (HREE) and pyroxene-poor of the peridotites suggest that the Dragon Bone mantle source was previously depleted in garnet stability field in an arc setting prior to or during the assembly of Gondwana.

2. Geological setting

The SWIR is a highly oblique ultra-slow spreading ridge with a full spreading rate of ~14 mm/year, extending 7700 km from the Bouvet to the Rodriguez Triple Junction. The ridge crosses over the northern side of the large southern oceans geoid high centered over Marion and Crozet islands and the Conrad Rise (Fig. 1A). This 3400 km portion of the SWIR is the Marion Rise, a large region of elevated ridge axis that represents a 2.1 km along-axis depth anomaly equal in size to the Icelandic Rise (Zhou and Dick, 2013). The Marion Rise steadily shoals from just east of the Melville FZ (Fracture Zone) to the Discovery FZ, where it plateaus all the way to the Prince Edward FZ before dropping precipitously across the Andrew Bain FZ.

The Dragon Bone amagmatic segment is located at 53°E Southwest Indian Ridge, approximately halfway between the Melville and the Discovery FZ's on the Marion Rise (Fig. 1A). It would be expected to have fairly thick crust if a mantle plume supports the rise as at Iceland (Weir et al., 2001). The segment was originally described as the Godzilla Megamullion, but as it turns out mantle rock is being emplaced simultaneously on either side of the rift mountain. Thus it has been renamed, as it does not represent a simple asymmetrically spreading ridge segment. The Dragon Bone amagmatic segment is nearly non-volcanic, representing essentially 100% tectonic accretion by direct exposure of the mantle to the seafloor. There partially serpentinized mantle peridotite is sampled over large regions from the rift valley floor to the rift mountains with only scattered basalts (Fig. 1B) (Zhou and Dick, 2013). However across the 107 km Gallieni FZ, the western adjacent ridge segment appears to be volcanically robust, with a crust up to ~10 km thick (Zhao et al., 2013).

In 2010 the R/V Dayangyihao of the China Ocean Mineral Research and Development Association surveyed the ~90 km long Dragon Bone amagmatic segment (Fig. 1). The rift valley lacks an axial neovolcanic high, and is ~3900 m deep near its center, plunging to >5000 m at the Gallieni FZ. For ~50 km, its western half is flanked by a series of parallel E–W domed ridges shoaling to 1000 to 2800 m depth. These are distinct from more regularly lineated, presumably volcanic, terrains to the southeast and northeast (Zhou and Dick, 2013). Along the western rift, tectonic blocks exposing mantle peridotite are actively emerging from beneath the valley floor to form this terrain (Fig. 1B), which was mapped for ~67 km to the south.

Eleven dredges and three television grabs collected ~1938 kg rocks from the rift valley and the northern and southern rift mountains. Seven stations, concentrated near the transform (Fig. 1B), contained serpentinized peridotite, while earlier the RV Marion Dufresne dredged a single dunite with basalt near the center of the rift valley. Only minor gabbro was sampled as veins in peridotites at two localities (D4-2, and D9), and in one large block from the eastern ridge-transform high (TVG2–3), consistent with the general scarcity of gabbro along the SWIR (Zhou and Dick, 2013). The Dayangyihao rock dredge and TV-grab locations are shown in Fig. 1B.

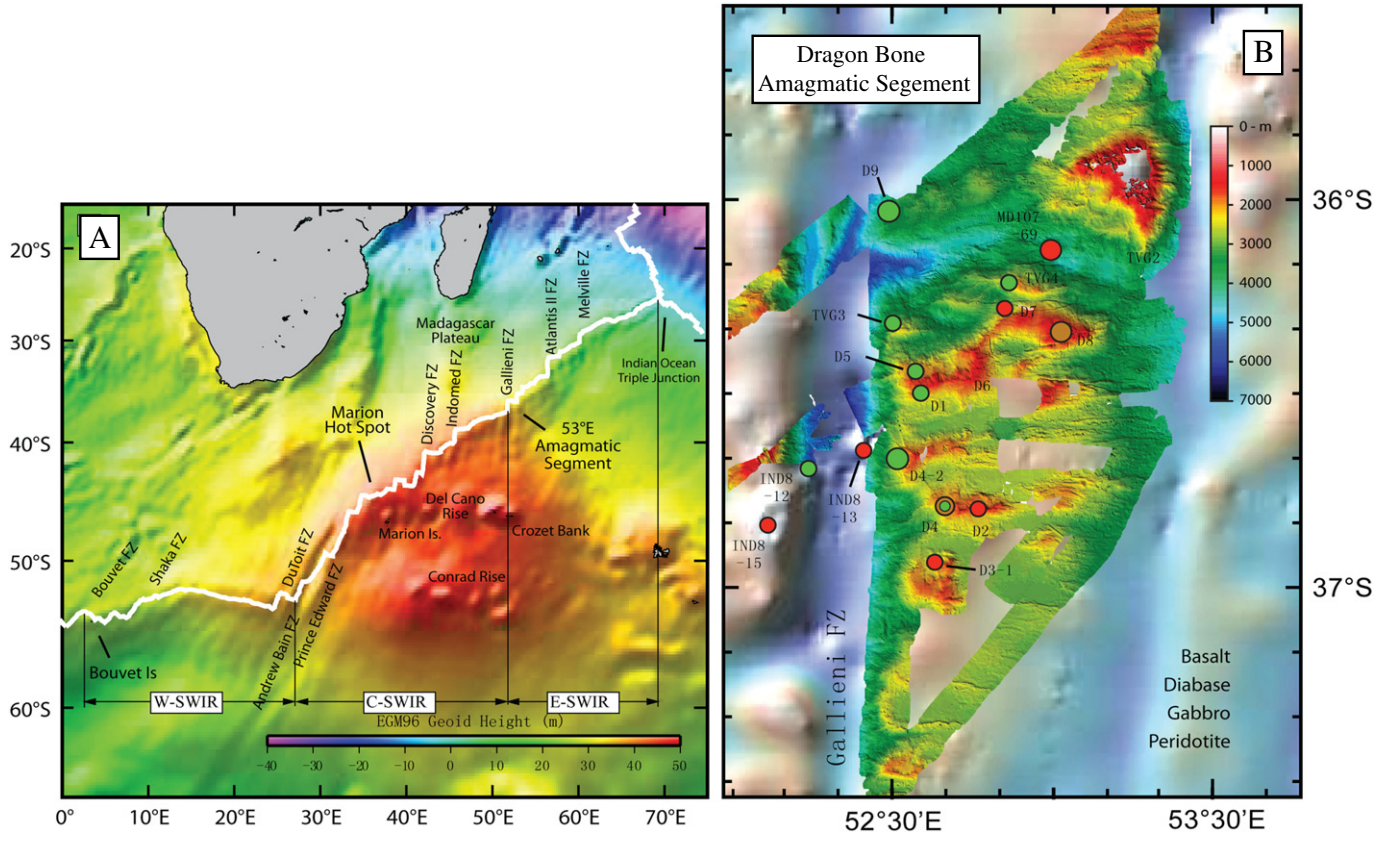

Fig. 1. A: Geoid map of the Southern Ocean plotted on a 0.25 * 0.25 degree grid; B: Seabeam map of the Dragon Bone amagmatic segment with sample locations modified from Zhou and Dick (2013). The green circles are peridotites; the red circles are basalts; and the orange circles are gabbros.

3. Samples and analytical methods

3.1. Samples

We selected 11 peridotites and 7 fresh non-glassy basalts for geochemical analysis. The peridotites are plagioclase-free spinel harzburgites with <5 vol.% diopside. They are moderately to strongly serpentinized, with rare relict olivine. Basalts are aphyric or plagioclase–olivine phyric; moderately or lightly weathered, but with no evidence of hydrothermal alteration.

3.2. Analytical methods

The outer portions of the samples, and any macroscopic veins were removed prior to processing in a corundum jaw crusher to <60 mesh. Sixty-gram sub-samples were powdered to <200 mesh in an agate ring mill. Major elements were determined by XRF at Guangzhou Institute of Geochemistry. Trace element compositions were measured at Wuhan the State Key Laboratory of Geological Processes and Mineral Resources. For the latter, samples were digested by HF + HNO_3 in Teflon bombs, and analyzed with an Agilent 7500a ICP-MS using Indium as the internal standard. An external standard was analyzed every ten samples to monitor secondary drift.

4. Results

4.1. Basalt geochemistry

Major and trace element data for seven basalts are listed in Table 1. The basalts have relatively evolved compositions with Mg# (molar 100 * Mg / (Mg + Fe)) from 40.7 to 66.0, and TiO_2 ranging from 1.07 to 2.09 wt.%. The average Dragon Bone MORB has 2.3 wt.% Na_2O and 0.18 wt.% K_2O. This is slightly less sodic and significantly less potassic than average SWIR MORB (average of 1180 SWIR Glasses: 3.34 wt.% ± 0.43 Na_2O, 0.34 wt.% ± 0.31 K_2O), which may be attributed to the seafloor weathering. Except D3-1-5 and D4, the trace element compositions of the Dragon Bone basalts are similar to typical N-MORB, and their REE patterns are all sub-parallel and slightly depleted in light REE relative to the middle REE (Fig. 2). D3-1-5 and D4 have incompatible trace element abundances ~50% lower than other samples, deplete in light REE and

Table 1
Major and trace element compositions of basalts from the Dragon Bone segment.

Sample	D7-1	D7-2	D7-3	D8	D4	D2	D3-1-5	TVG2-5	TVG2-3
Rock	B	B	B	B	B	B	B	G	G
Al_2O_3	15.1	16.1	15.1	15.1	18.3	15.1	17.9	17.6	18.9
CaO	10.8	8.48	11.3	10.3	12.2	11.3	11.8	12.9	19.4
FeOT	9.72	7.69	9.40	8.86	10.8	12.5	10.3	6.66	5.31
K_2O	0.18	0.22	0.096	0.19	0.21	0.17	0.25	0.049	0.013
MgO	6.99	6.31	7.02	9.55	4.12	5.10	5.10	9.90	7.64
MnO	0.15	0.18	0.16	0.18	0.18	0.19	0.15	0.15	0.12
Na_2O	3.21	4.15	2.94	3.09	2.69	3.03	2.72	2.67	0.94
P_2O_5	0.13	0.14	0.14	0.13	0.12	0.37	0.10	0.013	0.011
SiO_2	50.4	51.7	49.0	47.6	46.8	46.7	47.3	48.9	46.4
TiO_2	1.48	1.64	1.46	1.40	1.08	2.09	1.07	0.44	0.35
LOI	0.39	2.21	1.92	2.24	1.90	1.37	1.91	4.66	4.82
Total	99.7	99.7	99.7	99.7	99.6	99.4	99.7	100	99.6
Mg#	56.41	59.63	57.35	65.98	40.66	42.26	47.0	72.8	72.2
Sc	38.6	39.7	37.9	29.4	36.2	42.1	36.1	33.2	27.0
V	247	256	258	239	227	359	216	141	118
Cr	185	249	236	499	250	188	255	173	120
Co	40.2	49.4	39.3	50.6	57.6	38.9	53.2	38.2	26.5
Ni	84.5	107	111	188	128	67.8	140	95.9	76.9
Cu	63.0	64.4	21.1	18.7	125	86.6	121	219	23.1
Zn	76.2	78.5	62.6	63.8	89.0	151	94.3	59.7	39.4
Rb	2.23	2.21	0.66	1.47	4.73	1.76	5.23	0.44	0.23
Sr	151	135	120	146	155	166	147	118	31.0
Y	35.6	36.4	32.1	31.0	25.6	50.7	25.0	10.0	9.37
Zr	102	97.4	89.4	96.6	65.0	139	59.9	15.1	14.1
Nb	3.18	3.45	2.84	2.68	1.26	3.38	1.17	0.32	0.27
Cs	0.095	0.098	0.038	0.16	0.43	0.046	0.46	0.030	0.014
Ba	22.8	20.1	11.0	21.4	8.39	23.3	15.8	9.34	1.84
La	4.10	4.47	3.43	4.11	2.22	5.74	1.96	1.10	0.89
Ce	11.6	13.2	9.93	12.8	6.01	14.4	5.73	3.36	2.30
Pr	2.00	2.10	1.75	1.99	1.09	2.70	1.04	0.47	0.44
Nd	10.4	11.2	9.53	10.3	6.16	14.7	5.88	2.71	2.53
Sm	3.42	3.79	3.25	3.31	2.21	4.98	2.26	0.99	0.92
Eu	1.22	1.45	1.20	1.29	0.87	1.72	0.85	0.83	0.80
Gd	4.57	5.00	4.30	4.48	3.05	6.44	3.00	1.43	1.32
Tb	0.85	0.93	0.82	0.83	0.61	1.21	0.59	0.26	0.25
Dy	5.75	6.14	5.50	5.46	4.26	8.03	4.21	1.76	1.65
Ho	1.23	1.24	1.16	1.14	0.91	1.66	0.88	0.38	0.36
Er	3.57	3.66	3.30	3.18	2.67	4.84	2.60	1.05	0.98
Tm	0.51	0.53	0.46	0.47	0.42	0.70	0.38	0.15	0.15
Yb	3.29	3.16	2.96	3.15	2.69	4.47	2.58	0.96	0.94
Lu	0.50	0.47	0.43	0.44	0.41	0.70	0.40	0.15	0.15
Hf	2.55	2.65	2.38	2.44	1.68	3.73	1.61	0.50	0.50
Ta	0.21	0.22	0.20	0.18	0.091	0.22	0.090	0.033	0.032
Pb	0.71	5.37	0.76	3.92	1.28	3.30	0.76	1.80	0.23
Th	0.25	0.33	0.23	0.24	0.086	0.24	0.078	0.051	0.022
U	0.091	0.18	0.13	0.097	0.19	0.47	0.12	0.031	0.018

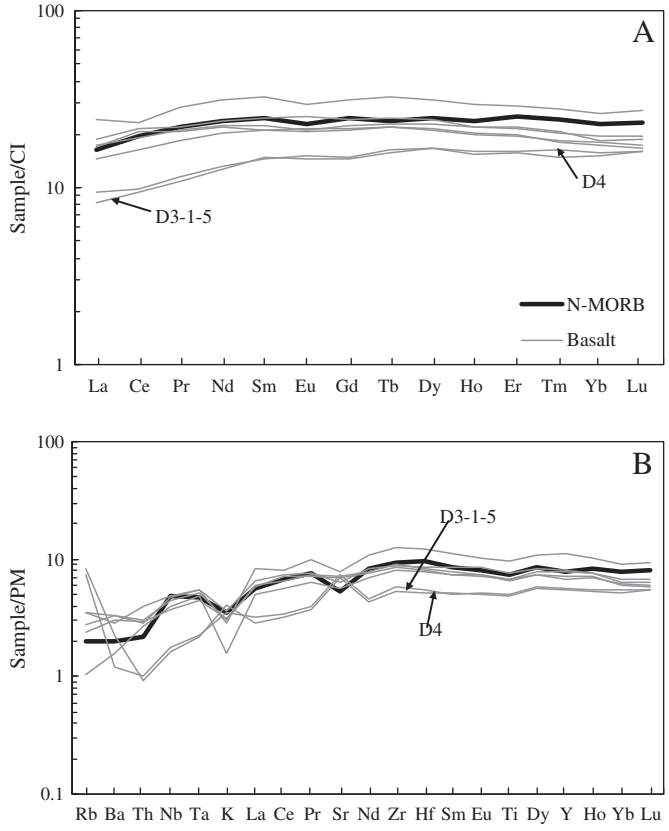

Fig. 2. (a) Carbonaceous chondrite (McDonough and Sun, 1995) and (b) primitive mantle (McDonough and Sun, 1995) normalized trace element abundances of the Dragon Bone basalts. N-MORB data is from Hofmann (1988).

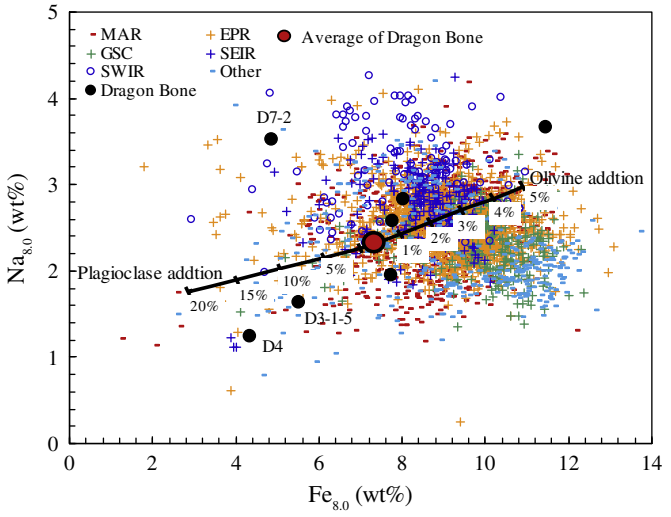

Fig. 3. $Na_{8.0}$ and $Fe_{8.0}$ variations of the Dragon Bone basalts compared to the mid-oceanic ridge basalts. MORB data are downloaded from PetDB and GeoRoc. GSC = Galapagos Spreading Center, SEIR = Southeast Indian Ridge, SWIR = Southwest Indian Ridge, MAR = Mid-Atlantic Ridge, EPR = East Pacific Rise.

have a flat middle REE and heavy REE pattern (Fig. 2a). Although the basalts are whole rock compositions rather than glasses, the depleted light REE patterns suggest the REE are unaffected by seafloor weathering. The relative abundances of the basalt REE are otherwise consistent with varying extents of fractional crystallization.

With the exception of D7-2, the basalts have positively correlated $Na_{8.0}$ and $Fe_{8.0}$ defining an orthogonal trend to the global MORB glass trend of Klein and Langmuir (1987). This is likely due to accumulation of plagioclase or olivine phenocrysts (Fig. 3). Moreover, our lowest $Na_{8.0}$ and $Fe_{8.0}$ samples (D4 and D3-1-5) have higher Al_2O_3 contents for a given MgO, indicating plagioclase accumulation. This explains the low REE contents of samples D4 and D3-1-5 as due to dilution by plagioclase. Higher K and Sr are preferentially partitioned into plagioclase in these samples (Fig. 2b). Sample D7-2 is an outlier in major element composition space; depleted in CaO, FeO^T, and enriched in K_2O and Na_2O relative to the other basalts. However, as its REE pattern is similar to other Dragon Bone basalts, we attribute this to alteration.

4.2. Peridotite whole rock chemistry

Peridotite volatile-free major element oxide and trace element compositions are listed in Table 2. Loss on ignition (LOI) ranges from 9.2 to 13.2 wt.%, consistent with the high degree of serpentinization and weathering seen in hand specimen. MnO ranges from 0.10 to 0.18 wt.%, within the abyssal peridotite range (Snow and Dick, 1995). Mg# varies from 88.4 to 91.1, with an average of 89.7 ± 0.7. However, the average olivine Mg# in 305 olivine-bearing spinel abyssal peridotites is 90.5 ± 1.0 (1σ), while pyroxene Mg#'s are about 1% higher. Therefore, many of our samples, and those abyssal peridotite whole rocks have clearly undergone Mg loss, likely due to weathering (Snow and Dick, 1995). Significant late basaltic melt impregnation can be excluded, due to the low whole rock Al_2O_3 and TiO_2 in the Dragon Bone peridotites.

The general effect of Mg-loss is to spread out the whole rock analyses in element–element plots along the Mg# axis (Fig. 4). This alone, however, cannot explain the consistent negative correlations of Al_2O_3, CaO and FeO^T with Mg#. These variations are expected for residues of varying degrees of mantle melting consistent with the modal and trace element data for other abyssal peridotites (Dick et al., 1984; Johnson et al., 1990). Notably, the Dragon Bone peridotites, and those peridotites from the west over the Marion Platform to the Andrew Bain Transform (C-SWIR), have consistently lower Al_2O_3 contents than peridotites from the rest of the Southwest Indian Ridge (Fig. 4a). A similar difference is evident for CaO in Fig. 4b, though there is more overlap, likely due to the mobility CaO during weathering and serpentinization. No significant differences for total FeO are present, possibly due to the mobility of iron during weathering and serpentinization which may have obscured any original differences in Fig. 4c.

4.3. Peridotite trace elements

In primary upper mantle (PUM) (McDonough and Sun, 1995) normalized multi-elements diagram (Fig. 5), the Dragon Bone peridotites are characterized by enrichment in highly incompatible elements. The peridotites also have positive anomalies for Zr and Sr relative to their neighboring elements. The enriched Rb, Sr, Ba and Zr show systematic variations with serpentinization, which could be attributed to the addition from seawater (Chen et al., 2015). The Dragon Bone peridotites also have a wide range of heavy REE abundances (<0.3 to >1.0 × chondrite), and an even more extreme range for light REE (e.g., La = 0.02 to 0.45 × chondrite), and are significantly lower than the depleted MORB mantle (DMM) of Salters and Stracke (2004) (Fig. 6).

Based on the REE patterns, the peridotites can be divided into two groups (Fig. 6). Group 1 samples have the lowest light REE contents with negative Eu anomalies and are more depleted in middle REE than in heavy REE (Fig. 6). Group 2 peridotites have less depleted middle REEs and less extreme positive strontium anomalies, but in other respects are similar to Group 1 (Figs. 5 and 6). The enriched light REE with Ce and Eu negative anomalies in Group 2 are similar with those in seawater (Fig. 6).

Table 2
Major and trace element compositions of peridotites from the Dragon Bone segment.

Sample	D1-5	D1-7	D1-14	D1-15	D1-10	D4-2-5	D4-2-4	D5-3	D5-4	D5-5	D5-6	D5-8	D6-3	D6-8	D9-5	D9-6	TVG3-2	TVG3-5	TVG3-8
Al_2O_3	1.51	1.37	1.69	1.67	1.63	2.03	1.80	1.86	1.81	1.80	1.94	1.22	1.36	1.30	1.37	1.08	1.97	2.19	2.44
CaO	0.51	1.29	1.76	1.86	1.66	1.77	0.11	1.01	1.45	0.72	1.39	0.081	0.40	0.54	1.42	0.80	1.38	1.62	1.57
FeOT	8.56	7.58	8.50	8.64	8.06	9.12	8.29	8.80	9.07	9.16	8.91	9.32	8.59	8.64	8.21	8.46	9.87	9.17	9.16
K_2O	0.037		0.022	0.026	0.039	0.074	0.022	0.008	0.015	0.039	0.009		0.027	0.029	0.032	0.009	0.025	0.039	0.052
MgO	43.0	43.3	39.5	39.3	41.2	38.6	43.0	41.6	38.5	41.4	40.4	44.3	43.1	43.0	39.8	41.6	39.9	38.9	38.0
MnO	0.12	0.12	0.12	0.11	0.098	0.13	0.19	0.11	0.21	0.17	0.20	0.13	0.18	0.15	0.13	0.16	0.12	0.12	0.15
Na_2O	0.38	0.078	0.17	0.18	0.28	0.47	0.17	0.12	0.19	0.20	0.11	0.078	0.21	0.17	0.24	0.16	0.34	0.40	0.40
P_2O_5	0.037	0.008		0.004	0.043	0.057	0.022	0.032	0.034	0.054	0.032	0.011	0.043	0.036	0.053	0.022	0.011	0.011	0.037
SiO_2	45.1	45.4	47.5	47.4	46.3	46.9	45.6	45.7	48.1	45.7	46.3	44.4	45.3	45.3	47.9	47.0	45.6	46.7	47.3
TiO_2	0.023	0.010	0.016	0.018	0.011	0.031	0.036	0.028	0.043	0.030	0.038	0.026	0.016	0.017	0.013	0.013	0.061	0.087	0.075
LOI	13.2	12.9	9.16	9.37	11.8	11.1	13.1	11.6	10.2	11.9	11.2	12.1	13.2	13.1	10.8	11.5	11.3	10.6	9.93
Total	99.2	99.2	99.2	99.2	99.3	99.3	99.2	99.3	99.4	99.2	99.3	99.5	99.2	99.2	99.2	99.2	99.3	99.3	99.2
Mg#	90.0	91.1	89.3	89.1	90.2	88.4	90.3	89.5	88.4	89.0	89.1	89.5	90.0	90.0	89.7	89.8	87.9	88.4	88.2
Sc	9.63	12.1	12.9	12.9	12.3	13.6	11.7	11.0	12.6	10.9	12.1	7.72	8.51	8.54	8.10	7.67	11.6	12.8	13.2
V	53.5	65.5	62.3	64.0	73.9	102	78.2	82.4	88.3	76.5	84.7	38.6	49.6	46.3	63.6	61.2	68.6	80.1	81.5
Cr	2276	3331	2755	2873	3146	2703	2707	2534	2335	2655	2453	1921	2221	2157	3165	2656	2429	2631	2959
Co	71.4	71.9	109	112	117	111	99.7	108	121	130	127	101	111	107	120	131	105	98.1	97.2
Ni	1747	1285	2153	2223	1811	1857	2006	2061	1645	2073	1932	1252	1865	2067	2358	2322	2093	2110	2173
Cu	36.7	19.3	14.2	16.6	22.5	119	46.8	23.0	46.1	37.9	53.0	33.1	38.9	27.3	9.41	25.5	3.43	9.22	2.70
Zn	69.5	77.2	42.6	43.2	65.3	260	112	63.9	112	98.7	98.1	88.3	107	83.5	66.0	85.5	48.0	54.1	53.0
Rb	0.30	0.053	0.34	0.50	0.28	0.52	0.31	0.19	0.26	0.22	0.20	0.11	0.18	0.15	0.22	0.23	0.31	0.32	0.44
Sr	3.27	2.63	10.3	7.12	5.03	7.16	7.67	4.45	8.52	5.00	6.04	3.57	4.34	3.35	56.4	15.3	29.3	5.93	5.93
Y	0.58	0.77	0.69	0.73	0.66	1.06	1.16	0.92	2.20	0.68	1.45	0.92	0.54	0.44	0.56	1.14	1.38	2.19	3.07
Zr	1.64	3.51	0.12	0.36	0.40	2.38	3.54	0.78	6.27	0.63	2.42	4.29	2.75	2.20	0.18	4.20	0.58	1.05	0.82
Nb	0.056	0.088	0.0071	0.014	0.024	0.035	0.37	0.063	0.27	0.026	0.12	0.13	0.055	0.035	0.032	0.27	0.13	0.26	0.21
Cs	0.022	0.0027	0.013	0.022	0.014	0.038	0.011	0.0058	0.014	0.020	0.0090	0.0029	0.017	0.018	0.014	0.0084	0.018	0.015	0.019
Ba	1.08	0.69	1.02	1.19	0.93	1.32	5.14	1.06	5.38	6.05	3.08	1.95	1.48	0.81	1.42	3.85	1.25	1.92	1.39
La	0.061	0.078	0.0048	0.018	0.068	0.094	0.57	0.100	0.94	0.078	0.42	0.38	0.11	0.077	0.13	0.77	0.26	0.35	0.34
Ce	0.033	0.46	0.011	0.034	0.11	0.11	3.06	0.15	4.30	0.19	1.46	1.67	0.053	0.21	0.054	3.50	0.61	1.05	1.19
Pr	0.016	0.022	0.0013	0.0054	0.018	0.023	0.12	0.027	0.20	0.017	0.096	0.080	0.029	0.021	0.028	0.18	0.082	0.17	0.21
Nd	0.069	0.083	0.010	0.018	0.077	0.097	0.45	0.11	0.81	0.076	0.40	0.33	0.12	0.086	0.12	0.79	0.31	0.87	1.05
Sm	0.024	0.025	0.0096	0.015	0.020	0.038	0.12	0.025	0.18	0.024	0.11	0.076	0.031	0.024	0.028	0.16	0.084	0.20	0.32
Eu	0.0070	0.0073	0.0033	0.0049	0.0050	0.012	0.036	0.0097	0.057	0.0080	0.027	0.023	0.010	0.0070	0.0080	0.046	0.071	0.13	0.16
Gd	0.043	0.046	0.026	0.029	0.041	0.075	0.14	0.057	0.29	0.049	0.14	0.12	0.049	0.037	0.035	0.21	0.11	0.29	0.41
Tb	0.0090	0.010	0.0079	0.0094	0.0090	0.016	0.026	0.014	0.049	0.010	0.027	0.021	0.0080	0.0070	0.0060	0.031	0.028	0.055	0.075
Dy	0.083	0.11	0.082	0.093	0.073	0.15	0.17	0.12	0.36	0.087	0.20	0.16	0.066	0.054	0.050	0.21	0.23	0.33	0.55
Ho	0.021	0.024	0.023	0.025	0.020	0.037	0.045	0.028	0.085	0.023	0.047	0.033	0.016	0.014	0.014	0.041	0.051	0.088	0.12
Er	0.070	0.079	0.082	0.085	0.068	0.12	0.14	0.11	0.27	0.073	0.16	0.097	0.055	0.045	0.046	0.12	0.15	0.25	0.34
Tm	0.013	0.015	0.015	0.014	0.012	0.021	0.018	0.017	0.040	0.013	0.026	0.016	0.0090	0.0080	0.0080	0.022	0.028	0.041	0.052
Yb	0.092	0.11	0.12	0.10	0.087	0.15	0.17	0.11	0.30	0.094	0.18	0.12	0.071	0.060	0.055	0.15	0.18	0.28	0.34
Lu	0.016	0.017	0.023	0.021	0.016	0.026	0.024	0.021	0.042	0.018	0.031	0.020	0.013	0.012	0.012	0.022	0.029	0.045	0.056
Hf	0.015	0.042	0.0056	0.013	0.0050	0.012	0.075	0.018	0.075	0.011	0.039	0.042	0.019	0.012	0.0040	0.064	0.022	0.025	0.024
Ta	0.0050	0.0066	0.012	0.011	0.0020	0.0020	0.014	0.014	0.017	0.0020	0.012	0.0097	0.0020	0.0010	0.0040	0.013	0.016	0.018	0.009
Pb	2.93	1.22	0.032	0.032	0.95	0.81	5.86	0.22	7.61	0.26	3.35	3.02	0.87	0.29	0.041	3.66	0.076	0.13	0.045
Th	0.014	0.021	0.0018	0.0054	0.0090	0.0050	0.081	0.0089	0.098	0.012	0.075	0.038	0.018	0.014	0.0040	0.13	0.016	0.031	0.028
U	0.49	0.63	0.076	0.14	0.85	0.49	0.44	0.53	0.42	0.48	0.49	0.54	0.53	0.45	0.97	0.88	0.40	0.38	0.45

P1 = Group 1 peridotite, P2 = Group 2 peridotite.

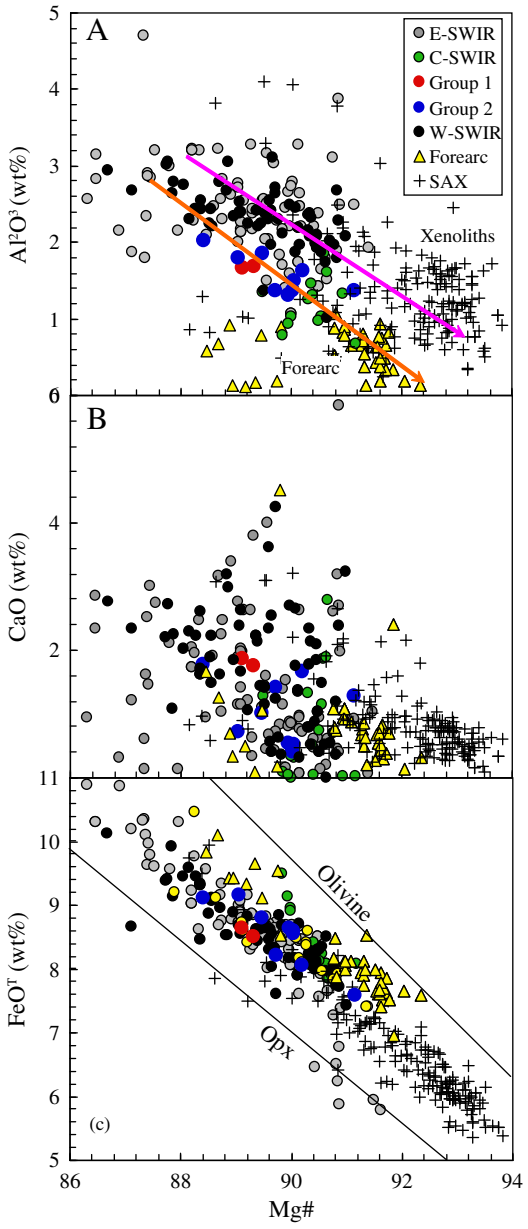

Fig. 4. Comparison of major element compositions of abyssal peridotites from the Dragon Bone amagmatic segment and Southwest Indian Ridge (Chen et al., 2015; Niu, 2004; Snow and Dick, 1995; Zeng et al., 2012), the forearc peridotites (Parkinson and Pearce, 1998; Pearce et al., 2000) and South Africa Xenoliths (Boyd et al., 2004; Grégoire et al., 2003; Grégoire et al., 2005; Griffin et al., 2004; Herzberg et al., 1988; Kuskov et al., 2006; Maier et al., 2005; Simon et al., 2003). W-SWIR = Bouvet FZ to Andrew Bain FZ, C-SWIR = Andrew Bain FZ to Gallieni FZ, E-SWIR = Gallieni FZ to Rodriguez Triple Junction, SAX = South Africa Xenoliths. The pink and orange arrow in (a) is sketching for the dry and wet melting, respectively; The Olivine and Opx lines are summary of their compositions from literatures.

4.4. Peridotite spinel chemistry

Zhou and Dick (2013, Supplementary data Table III) report analyses of 16 peridotites from the Dragon Bone amagmatic segment and another 10 from the western wall of the adjacent Gallieni FZ. Spinel Cr# (molar 100 * Cr / (Cr + Al)) from the Dragon Bone segment lie systematically to the low Mg# side of the abyssal spinel array (Fig. 7a) with an average composition more iron rich and slightly more aluminous than those for the segment immediately west of the Gallieni FZ. These reflect a somewhat lower degree of mantle melting. If the difference in FeO^T and Al_2O_3 contents were due to refertilization by a MORB-like melt, there should be a corresponding elevation in Al_2O_3 and CaO, and especially TiO_2 (Dick, 1989). The spinel TiO_2 compositions range from 0.02 to 0.13 wt.%, well within the range for simple residues of mantle melting with minimal late-stage melt impregnation (Dick and Bullen, 1984) (Fig. 7b).

5. Discussion

We have complementary data for abyssal peridotites and spatially associated basalts that reflect a wide range of processes from the mantle to seafloor. Assuming symmetrical spreading at ~14 mm/year, the Dragon Bone peridotites were emplaced to the seafloor at <5.5 Ma, significantly later than eruption of our basalt samples. Thus they were deep in the lithosphere when most of the Dragon Bone basalts erupted, and are therefore plausible residues for the basalts. The peridotites, however, are strongly serpentinized and weathered — processes that clearly involve significant elemental fluxes. Experimental and empirical studies on peridotite alteration suggest that serpentinization can, in some cases, be isochemical except for the addition of seawater, weathering of relict olivine and pyroxene systematically extracts Mg from the rock (Agranier et al., 2007; Coleman and Keith, 1971; Jöns et al., 2010; Snow and Dick, 1995). The addition of seawater and serpentinization may enrich the incompatible elements in abyssal peridotites, including the LREE and LILE (Chen et al., 2013, 2015). Middle and heavy REE, however, are often resistant to serpentinization and seafloor weathering (Blundy et al., 1998; Hellebrand et al., 2001; Johnson, 1998; Niu, 2004; Salters and Longhi, 1999). While REE contents can be significantly modified by late melt impregnation, this is easily recognizable as it produces a noticeable deviation of the REE pattern. The melt impregnation can also be screened by monitoring accessory chrome spinel, where elevated TiO_2 is generally diagnostic of melt addition (Fig. 7b). Therefore, after screening our analyses for melt addition, middle and heavy REE patterns of the least-altered the Dragon Bone peridotites were modeled using the starting compositions and mineral–melt partition coefficients in Table 3.

Given the problems in estimating the primary mineral compositions of abyssal peridotites (Dick et al., 1984), we concentrate here on geochemistry. Whole rock chemistry, though it incorporates the effects of alteration, may be the best way to obtain the primary concentrations of relatively immobile elements such as Al_2O_3, chrome, and the middle and heavy REE. Accordingly, these elements provide the best opportunity to interpret the origin of highly altered peridotites for whole rock compositions. Moreover, we use the major element composition of chromium spinel, collected previously, to supplement the information obtained from our whole rock data.

5.1. Mantle source and melting process

5.1.1. A pyroxene poor mantle source of Marion Rise

The major and trace element composition of the Dragon Bone peridotites is generally consistent with residues of varying degree's of mantle melting as inferred from the modal and mineral data for abyssal peridotites (Dick et al., 1984; Johnson et al., 1990). Characteristically Al_2O_3, CaO, and FeO^T decrease with increasing Mg# (Fig. 4). Such a general trend can be seen in the whole rock data for the Southwest Indian Ridge (Fig. 4). However, the data show broad scatter that cannot be simply attributed to the partial melting. Relict olivine and pyroxene in abyssal peridotites have a restricted composition with respect to Mg#, which ranges from $Fo_{89.5}$ to $Fo_{91.5}$ for olivine, and is shifted to about 1% higher for pyroxenes. Thus data plotting at lower Mg# must be due to Mg-loss during alteration and weathering. Similarly CaO is highly mobile during alteration, with enrichment due to carbonate precipitation and depletion due to weathering and serpentinization. Therefore we restrict interpretation of the data in Fig. 4 to samples whose Mg# lies above 89.5. Moreover, we exclude samples for which CaO lies significantly below or above the main abyssal peridotite trend due to its

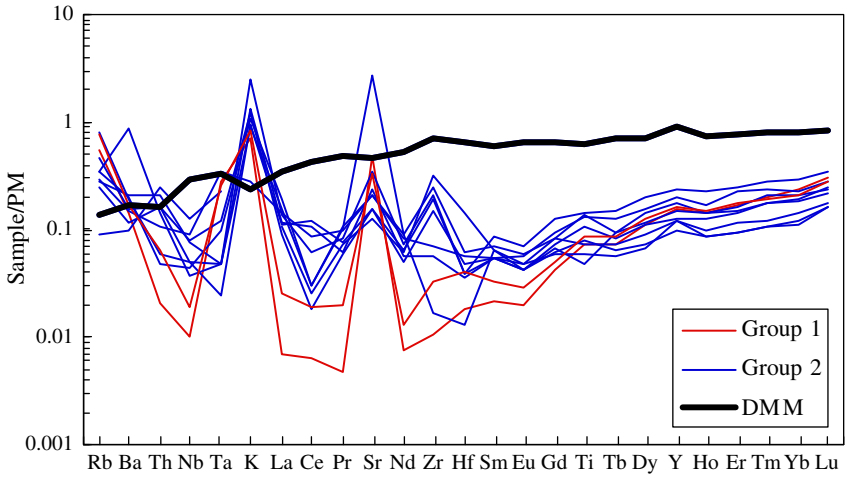

Fig. 5. Primitive upper mantle-normalized (McDonough and Sun, 1995) trace element abundances of abyssal peridotites from the Dragon Bone amagmatic segment. Depleted MORB mantle (black line) (Salters and Stracke, 2004) is also shown for comparison.

mobility. This excludes the majority of the data from the Dragon Bone segment in the recent study of Chen et al. (2015).

The Dragon Bone peridotites are similar in Al_2O_3 and CaO contents to those of the Marion Platform between the Gallieni and Andrew Bain FZ (C-SWIR). These Al_2O_3, and CaO contents are lower on average at the same Mg# than for abyssal peridotites from west of the Andrew Bain Transform (W-SWIR), and those east of the Dragon Bone segment (E-SWIR). As CaO and Al_2O_3 are largely resident in diopside and enstatite, the C-SWIR residual mantle has significantly less Al_2O_3 and CaO and hence lower pyroxene content than residual peridotites from the eastern and western SWIR. Partial melting drives the bulk composition of a peridotite along a straight trend of decreasing CaO and Al_2O_3 with increasing Mg# away from the olivine–diopside–enstatite cotectic. This cotectic has a different position in ten-component major element space for each unique mantle composition. If the mantle source has a fairly uniform composition, then the trend will be tight, and will project back to a restricted initial source composition. If there is substantial variation in the source, the trend will be broad, as the position of the cotectic will vary. If one source is significantly different than another, then melting will generate two separate, but parallel trends as we can actually see in Fig. 4.

The significant differences in CaO and Al_2O_3 at the same Mg#s of the central SWIR from the eastern and western SWIR then indicate two discrete melting trends, one for the eastern and western SWIR, and another for the central SWIR. This indicates different source compositions at the Marion Platform which has an anomalously depleted Al_2O_3-poor source composition (Fig. 4). In the garnet stability field, there is a substantial density difference between Al_2O_3 poor harzburgites, and Al_2O_3-rich lherzolites due to the high density of natural pyrope garnet (~3.73 g/cm^3, ~22 wt.% Al_2O_3). However, spinel harzburgites and lherzolites have very similar density (~3.3 g/cm^3) in the lower pressure spinel peridotite field (Dick, 1989). This provides a direct evidence that an Al_2O_3-poor buoyant mantle source supports the elevated bathymetry of the Marion Rise as previously suggested based on the geologic evidence for thin or missing crust on the Marion Platform (Zhou and Dick, 2013), it also requires a thick depleted layer in the mantle in the garnet stability field that could extend down to the transition zone.

5.1.2. The Dragon Bone peridotites are residuals of wet melting

Chromium spinel is a well-established petrogenetic indicator for mantle peridotites (Dick and Bullen, 1984; Irvine, 1967). This is fortunate as due to elemental fluxes, most whole-rock major element modeling approaches are not viable for extensively altered abyssal peridotites. Spinel in peridotites is resistant to both weathering and serpentinization, but its composition is strongly affected by subsolidus reequilibration, and is a function of cooling rate and the relative proportion of silicates to spinel (Irvine, 1967). The Dragon Bone data is for accessory spinel

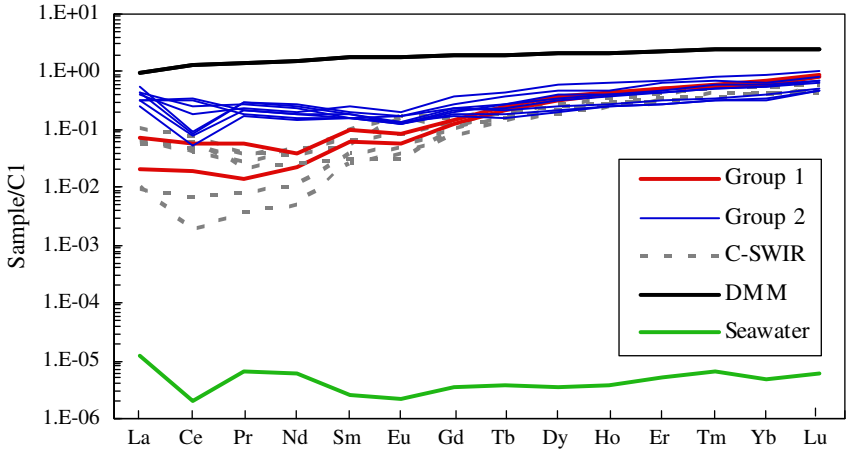

Fig. 6. Carbonaceous Chondrite-normalized (McDonough and Sun, 1995) REE abundances for the Dragon Bone peridotites.

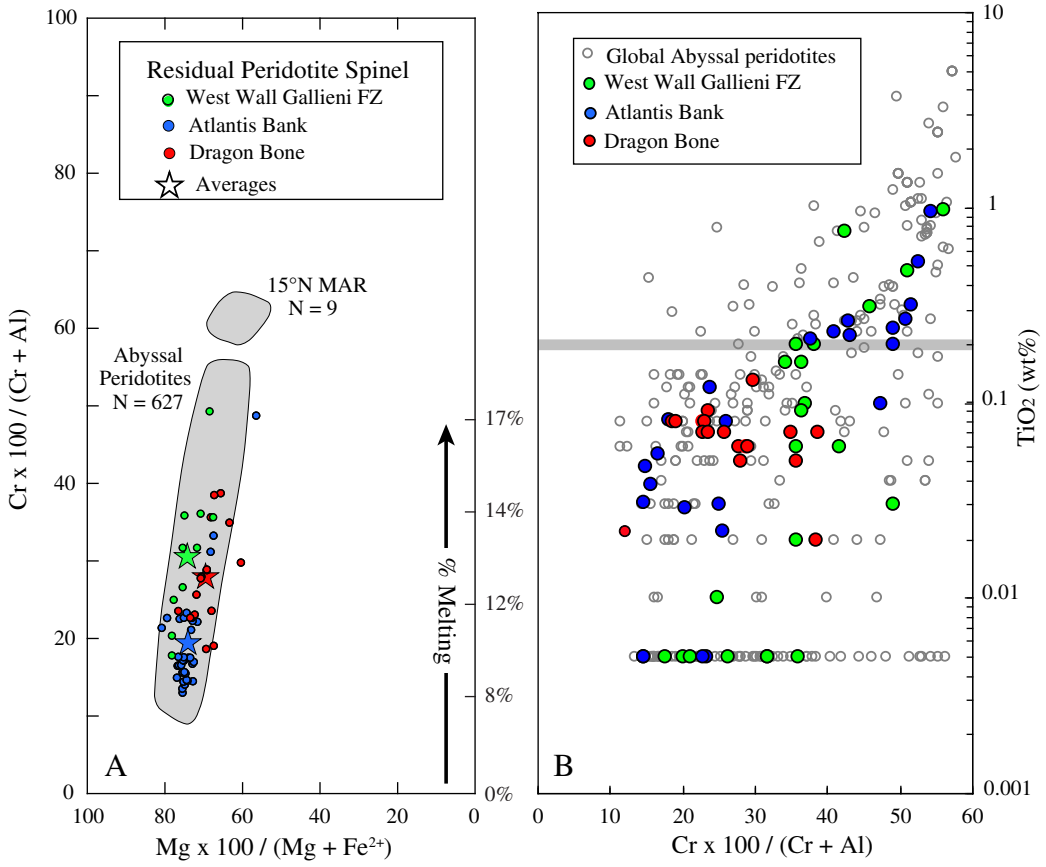

Fig. 7. Comparison of Cr# with Mg# and TiO_2 of spinels from the Dragon Bone amagmatic segment peridotites (Zhou and Dick, 2013) and spinel analyses for earlier dredges in SWIR from Dick unpublished data.

(<1 vol.%). This means that differences in spinel composition are due to different diffusion closure temperatures, or to systematic differences in the peridotite bulk composition. As peridotites dredged from the MAR and SWIR were all emplaced at the ridge axis over a relatively narrow range of seafloor spreading rate and hence mantle upwelling rates, the closure temperature should be relatively constant. Thus spinel

Table 3
Melting model: input parameters.

	Distribution coefficients[a]					Source composition[b]	
	Ol/M	Cpx/M	Opx/M	Sp/M	Grt/M	PUM	DMM
La	0.0067	0.056	0.0053	0.0003	0.0014	0.648	0.234
Ce	0.0060	0.092	0.009	0.0005	0.0029	1.675	0.772
Pr	0.0060	0.161	0.0127	0.0007	0.0083	0.254	0.131
Nd	0.0059	0.303	0.0163	0.0008	0.03	1.250	0.713
Sm	0.0067	0.445	0.020	0.0009	0.18	0.406	0.27
Eu	0.0074	0.5005	0.0275	0.0010	0.33	0.154	0.107
Gd	0.0095	0.556	0.035	0.0011	0.75	0.544	0.395
Tb	0.0115	0.570	0.048	0.0013	1.5	0.099	0.075
Dy	0.0154	0.582	0.061	0.0018	2.4	0.674	0.531
Ho	0.0193	0.5825	0.074	0.0023	3.7	0.149	0.122
Er	0.0256	0.5830	0.0838	0.0030	4.4	0.438	0.371
Tm	0.0374	0.5625	0.0935	0.0038	6.0	0.068	0.06
Yb	0.0491	0.542	0.1033	0.0045	6.5	0.441	0.401
Lu	0.06	0.506	0.113	0.0050	6.7	0.0675	0.063

	Source modes[c]		Melt modes[d]	
	Grt-per	Sp-per	Grt-per	Sp-per
Ol	0.57	0.53	0.04	−0.06
Cpx	0.13	0.17	1.05	0.67
Opx	0.21	0.27	−0.19	0.28
Sp	0	0.03	0	0.11
Grt	0.09	0	0.11	0

[a] The partition coefficients of Ol, Cpx, Opx and Sp are from Niu and Hekinian (1997) and reference there in; the partition coefficients of Garnet from Green et al. (2000).
[b] The composition of PUM is from McDonough and Sun (1995) and DMM from Salters and Stracke (2004).
[c] The source modes of minerals are from Johnson et al. (1990).
[d] Melt model of garnet peridotites is from Walter (1998) and melt model spinel peridotites is from Ghiorso et al. (2002).

compositions in Fig. 7 should reflect systematic differences in rock compositions.

Chrome contents in abyssal peridotite spinels increase with decreasing modal diopside and increasing olivine Mg# as expected for mantle residues (Dick, 1989; Dick and Bullen, 1984), and are widely used to calculate the degree of melting (Hellebrand et al., 2001). The increase in chrome with decreasing Mg# in Fig. 7 reflects the relative effects of chrome and Al_2O_3 on the partitioning of Fe and Mg between spinel and olivine, and is parallel to the trend anticipated for mantle melting (Dick and Bullen, 1984). Peridotite spinels in Fig. 7 exhibit considerable scatter in Cr#, which reflects stochastic variations in local melt flux through these rocks during mantle melting and late-stage melt–rock reaction (Dick et al., 2010). When peridotite spinel compositions are averaged to reflect the overall local mantle composition, however, they

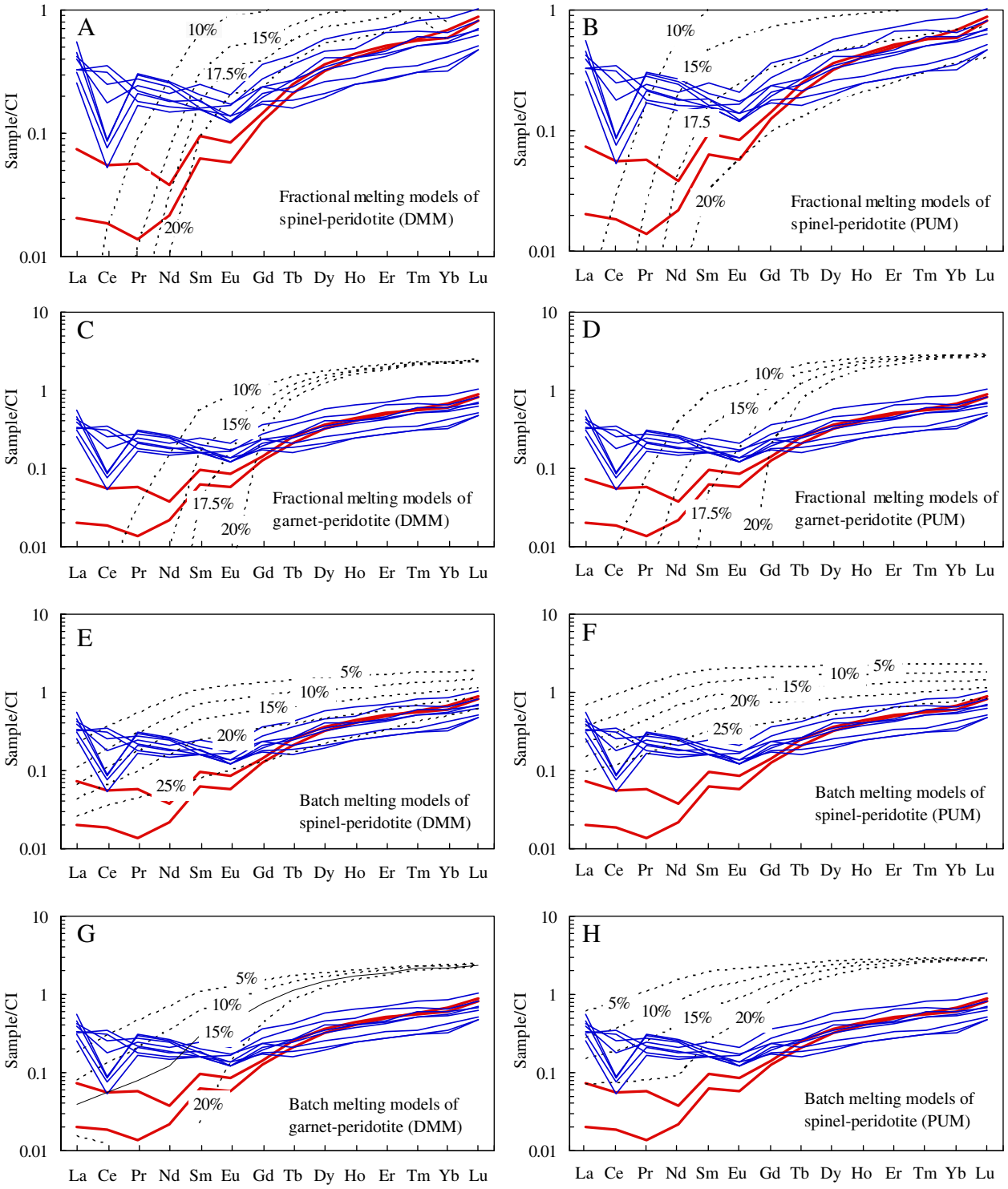

Fig. 8. Comparison of Chondrite-normalized (McDonough and Sun, 1995) REE patterns of the Dragon Bone peridotites with modeling residuals by fractional and batch melting with a primitive upper mantle (PUM) (McDonough and Sun, 1995) and a depleted MORB mantle source (DMM) (Salters and Stracke, 2004). The red lines are Group 1 samples and the blue lines are Group 2 samples. The model function and parameters are showing in Table 3.

show a consistent systematic correlation with the composition of spatially associated MORB reflecting variations in the degree of melting (Dick et al., 1984).

The average composition of the Dragon Bone spinels (Cr# ~ 27.7) are considerably more depleted than that for Atlantis Bank (Cr# ~ 22), 580 km to the northeast, which lies low on the Marion Rise at 57°E. Assuming similar mantle source compositions, this would correspond to ~4% more melting of a PUM source from east to west up to the edge of the Marion Platform (Zhou and Dick, 2013). However, the Dragon Bone spinel Cr#'s lie in the middle range of abyssal peridotites, which would indicate moderately aluminous pyroxene. Thus, without other evidence, the composition of the Dragon Bone mantle would seem to lie within the normal abyssal range, which would be inconsistent with a mantle sufficiently depleted to explain the extreme elevation of the Marion Rise. This assumes that the spinel composition is linked directly to mantle depletion, as in the correlation of Hellebrand et al. (2001) for dry melting. The amount of pyroxene in a residual peridotite, however, is not directly linked to the relative activities of chrome and Al_2O_3. At a first order, it is linked to the composition of the liquid being removed, which is very different for wet and dry conditions, as discussed by Dick and Bullen (1984). Specifically, melting under wet conditions in an arc-mantle wedge would produce more silica rich melts such as high-magnesian andesites and boninites (Kushiro, 1969). This would deplete a mantle residue in pyroxene components more rapidly than would be anticipated from the relative activities of chrome and Al_2O_3 in the peridotite. As the wet and dry cotectics lie on opposite sides of the diopside–enstatite join in the system silica–diopside–olivine (Kushiro, 1969), the complementary residues will then be correspondingly pyroxene poor and pyroxene rich. The pyroxene and Al_2O_3 poor mantle can also be due to the high temperature melting, while Zhou and Dick (2013) suggest that the Marion Rise is an isostatic response to low-density depleted mantle beneath the Southwest Indian Ridge rather than a large thermal anomaly (such as plume).

Partial melting trends in Al_2O_3–MgO and CaO–MgO plots generally follow a \ tight straight trend, similar to the red arrows in Fig. 4a. If the mantle source compositions are different, then the trends will be offset sub parallel from one another. For example, the xenolith suite, representing Archean mantle from beneath southern Africa, has a different source composition than the fore-arc peridotites. Similarly, the Marion Platform and the Dragon Bone segment must have a different initial source composition compared to the SWIR to the west and east. The question arises as to the origin of an anomalously pyroxene depleted initial source composition for the Central Southwest Indian Ridge. There is little indication that the current melting event at the central SWIR is producing anything other than MORB. Moving a peridotites composition off one trend to another is difficult, requiring removal of a different melt composition situated at a different cotectic point under different physical conditions. For dry melting, this cannot easily occur, which would make it difficult to explain the two SWIR trends. However, adding water to the system and wet melting can have a dramatic effect. Thus, we propose that the mantle beneath the central SWIR is the residue of an earlier wet melting event in an arc related terrains.

As can be seen in Fig. 4, the central SWIR peridotites are less depleted than fore-arc peridotites, but generally lie co-linear with them. Since the fore-arc peridotites represent the top of the melting column and thus end point for melting in an island arc. This suggests the central SWIR peridotites representing a deeper less depleted section of an arc mantle wedge. By contrast, the eastern and western SWIR peridotites could represent a source composition similar to Archean South African mantle xenoliths. Thus, considering alternative hypotheses for the source of the Central Southwest Indian Ridge basalts, it cannot be old Archean mantle, nor can it be normal oceanic asthenosphere as is the case to the East and West, but instead may correspond to the Neoproterozoic arc terranes of the East African Orogenic belt (Dick and Zhou, 2015).

5.1.3. Continuous melt extraction of the Dragon Bone peridotites by REE modeling

We compared the composition of the Dragon Bone peridotites with simple model residues of fractional and batch melting of DMM and PUM in the spinel stability fields (Fig. 8). Proportions of minerals going into the melt and the resulting melting-reaction function were determined using pMELTS (Ghiorso et al., 2002). The modeling shows that the Group 2 peridotites can be matched well by 15 to 20% melt extraction in the spinel peridotite stability field (Fig. 8b). The Group 1 peridotites, however, are inconsistent with simple melting residues, as modeling always over predicts middle REE concentrations for the observed heavy REE (Fig. 8a, b, e and f).

Experimental data and theoretical considerations show that the heavy REE are highly compatible in the garnet (Green et al., 2000). Therefore, calculations for melting in the garnet stability field were made using a melting reaction from Walter (1998). However, both the concentration and patterns of middle and heavy REE are poor fitting to the model residuals (Fig. 8c, d, g and h). Therefore, we tried a multi-stage model, first melting in the garnet stability field, and then melting the residues in the spinel field. The result shows that 7% fractional melting in the garnet field, followed by an additional ~12.5% or 13.5% fractional melting in the spinel field of DMM or PUM fit the Group 1 middle and heavy REE patterns well (Fig. 9). This is consistent with Heinonen et al.'s findings that some Karoo basalts from Antarctica show evidence of hydrous melting of a garnet peridotite source and Sr, Nd, Pb, Os, and He isotopic evidence of derivation from SWIR MORB sources (Heinonen and Kurz, 2015; Heinonen and Luttinen, 2010; Heinonen et al., 2010).

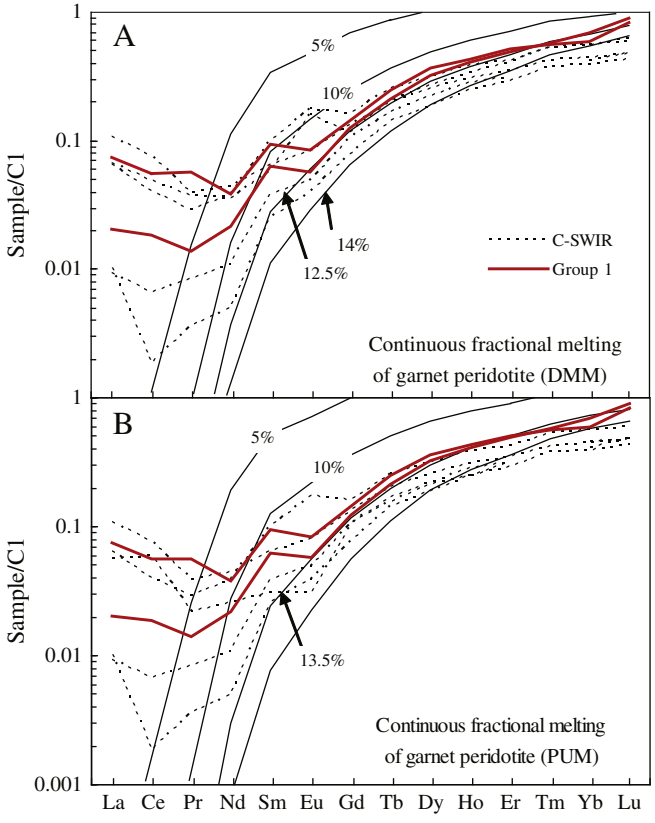

Fig. 9. Comparison of Chondrite-normalized (McDonough and Sun, 1995) REE patterns of the Dragon Bone Group 1 peridotites with residuals from the continuous fractional melting of garnet peridotite with a primitive upper mantle (PUM) (McDonough and Sun, 1995) and a depleted MORB mantle source (DMM) (Salters and Stracke, 2004). The garnet peridotite is 7% fractional melting in garnet stable field and then fractional melting in the spinel stable field. The model function and parameters are showing in Table 3.

The melts parental to the Dragon Bone basalts can be explained by about 5 to 10% non-modal equilibrium batch melting of DMM (Fig. 10a). As shown in Fig. 10, the REE compositions of liquids predicted from either melting model (Fig. 10c) or the actual peridotite (Fig. 10d) do not match those of the spatially associated basalts. This is generally case for abyssal peridotites (Johnson and Dick, 1992; Johnson et al., 1990). However, the modeling melt extraction may occur late in the melting column rather than throughout it (Kelemen et al., 1997), likely near the asthenosphere lithosphere boundary (Dick and Zhou, 2015). Five to 10% melting of DMM while typical for many regions with normal crustal thickness appears inconsistent with the small volume of erupted basalt at the Dragon Bone. As discussed above, the Dragon Bone mantle source was unusually poor in pyroxene, the decoupled composition of basalts and peridotites can be explained by the low-degree focused melting (Dick and Zhou, 2015). With focused melting the volume of mantle producing the Dragon Bone basalts at the early stages would be significantly expanded, while the actual degree of melting substantially reduced. Thus a pyroxene-poor mantle could produce a fairly typical looking MORB while producing only a small volume of basalt. Without focused melting, where melt and mantle react over most of the mantle melting column, producing tholeiitic rather than alkali basalt.

5.2. Ancient melting a way to reconcile the geochemical composition with geologic observation

Our REE modeling results indicate that the Dragon Bone peridotites would be residues of a moderately high degree of melting for either an assumed PUM or DMM source. Based on similar calculations for other regions of the global ridge system, the moderately high degree of melting predicts slightly greater crustal thickness than normal. This is also expected from the Dragon Bone peridotite spinel compositions, which are similar to the Marion Platform peridotites to the west. The average spinel Cr# (27.7) of the Dragon Bone peridotite is slightly lower than that observed at 23°N (Cr# of ~32) on the Mid-Atlantic Ridge at the southern end of the Azores Rise (Dick et al., 2010). Detrick and Purdy (1980) report a detailed seismic refraction experiment that gives 4 to 5 km crustal thickness in the same region south of the Kane FZ. Similarly, the average $Na_{8.0}$ of 2.3 wt.% of the Dragon Bone basalts lies within the range of typical EPR and MAR, consistent with a crustal thickness of ~6 km (Klein and Langmuir, 1987). Therefore, we would anticipate a crustal thickness at the Dragon Bone on the Southwest Indian Ridge of ~4 to 6 km, if the mantle source were similar to other ocean ridges.

However, the Dragon Bone segment has been nearly amagmatic. The segment does not have the crustal thickness that would be inferred from either the peridotite or basalt chemistry. The mantle source here and along the Marion Platform to the west has a composition atypical of presumed abyssal mantle parents such as PUM or DMM. Based on the whole rock data, the simplest and most direct explanation, for the missing crust at the Dragon Bone, is that the mantle source composition at the Dragon Bone was previously depleted in basaltic components by an earlier mantle melting event prior to or during the closure of the Mozambique Ocean in the Neproterozoic, and the subsequent assembly of Gondwana.

6. Conclusions

The composition of the mantle source beneath the Marion Platform and the Dragon Bone amagmatic segment was significantly more depleted in basaltic components than that for the Southwest Indian Ridge to the east and west. It has significantly lower bulk pyroxene and Al_2O_3 contents, and therefore lower density in the garnet stability

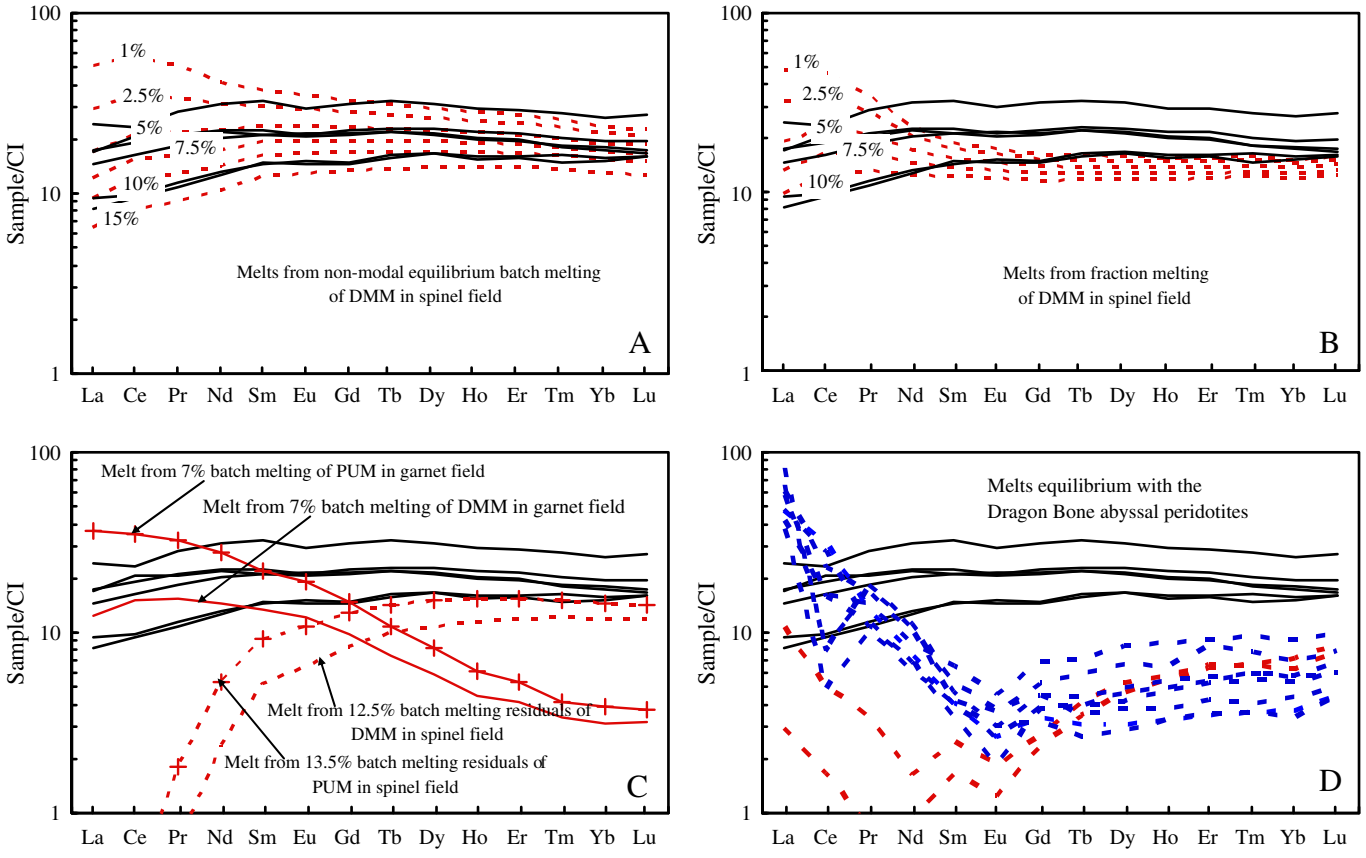

Fig. 10. Chondrite-normalized (McDonough and Sun, 1995) REE abundances for the Dragon Bone basalts compared with REE in melts from non-modal equilibrium batch melting (a) and fractional melting of DMM (b), melts from the first and second stages fractional melting of DMM and PUM (c), and calculated melts equilibrium with the Dragon Bone peridotites (d). The model function and parameters are showing in Table 3.

field. This provides direct evidence for the hypothesis that the Marion Rise is supported by atypically depleted buoyant asthenosphere. The spinel Cr# and REE compositions suggest that the Dragon Bone peridotites are residuals from a moderately high degree melting. The thin and discontinuous crust over the Marion Rise is inconsistent with such extensive melting during the present ridge event. Thus, the depletion of the Marion Platform asthenosphere represents an earlier hydrous mantle melting that began in the garnet peridotite prior to or during the closure of the Mozambique Ocean in the Neproterozoic, and the subsequent assembly of Gondwana.

Acknowledgments

This work was supported by the National Natural Science Foundation of China (Grant No. 41203024), the Chinese National Key Basic Research Program (2012CB417300), the Internationa Postdoctoral Exchange Fellowship Program and by the US National Science Foundation grant 1155721. We would like to acknowledge our colleagues Chenguang Sun, Horst Marschall, Nobu Shimizu, and Jixing Wang. We would also like to thank the editor, Andrew Kerr, and helpful reviews by Jussi S. Heinonen and an anonymous reviewer.

Appendix A. Supplementary data

Supplementary data to this article can be found online at http://dx.doi.org/10.1016/j.lithos.2015.12.007.

References

Agranier, A., Lee, C.T., Li, Z.X., Leeman, W.P., 2007. Fluid-mobile element budgets in serpentinized oceanic lithospheric mantle: insights from B, As, Li, Pb, PGEs and os isotopes in the feather river ophiolite, California. Chemical Geology 245, 230–241.

Alard, O., Luguet, A., Pearson, N.J., Griffin, W.L., Lorand, J.P., Gannoun, A., Burton, K.W., O'Reilly, S.Y., 2005. In situ Os isotopes in abyssal peridotites bridge the isotopic gap between MORBs and their source mantle. Nature 436, 1005–1008.

Blundy, J.D., Robinson, J.A.C., Wood, B.J., 1998. Heavy REE are compatible in clinopyroxene on the spinel lherzolite solidus. Earth and Planetary Science Letters 160, 493–504.

Boyd, F.R., Pearson, D.G., Hoal, K.O., Hoal, B.G., Nixon, P.H., Kingston, M.J., Mertzman, S.A., 2004. Garnet lherzolites from Louwrensia, Namibia: bulk composition and P/T relations. Lithos 77, 573–592.

Brandon, A.D., Snow, J.E., Walker, R.J., Morgan, J.W., Mock, T.D., 2000. ^{190}Pt–^{186}Os and ^{187}Re–^{187}Os systematics of abyssal peridotites. Earth and Planetary Science Letters 177, 319–335.

Chen, Z.Q., Zhou, H.Y., Liu, Y., Yang, Q.H., Li, J.W., Dick, H.J.B., 2013. Influence of igneous processes and serpentinization on geochemistry of the Logatchev Massif harzburgites (14 degrees 45′ N, Mid-Atlantic Ridge), and comparison with global abyssal peridotites. International Geology Review 55, 115–130.

Chen, L., Chu, F.Y., Zhu, J.H., Dong, Y.H., Yu, X., Li, Z.G., Tang, L.M., 2015. Major and trace elements of abyssal peridotites: evidence for melt refertilization beneath the ultraslow-spreading Southwest Indian Ridge (53° E segment). International Geology Review 1–20.

Coleman, R.G., Keith, T.E., 1971. A chemical study of serpentinization—Burro Mountain, California. Journal of Petrology 12, 311–328.

Detrick, R.S., Purdy, G.M., 1980. The crustal structure of the kane fracture zone from seismic refraction studies. Journal of Geophysical Research: Solid Earth 85, 3759–3777.

Dick, H.J.B., 1989. Abyssal peridotites, very slow spreading ridges and ocean ridge magmatism. Geological Society, London, Special Publications 42, 71–105.

Dick, H.J.B., Bullen, T., 1984. Chromian spinel as a petrogenetic indicator in abyssal and alpine-type peridotites and spatially associated lavas. Contributions to Mineralogy and Petrology 86, 54–76.

Dick, H.J.B., Natland, J.H., 1996. Late-stage melt evolution and transport in the shallow mantle beneath the East Pacific Rise. Proceeding of the Ocean Drilling Program, Scientific Results 147, 103–134.

Dick, H.J.B., Zhou, H.Y., 2015. Ocean rises are products of variable mantle composition, temperature and focused melting. Nature Geoscience 8, 68–74.

Dick, H.J.B., Fisher, R.L., Bryan, W.B., 1984. Mineralogic variability of the uppermost mantle along mid-ocean ridges. Earth and Planetary Science Letters 69, 88–106.

Dick, H.J.B., Lissenberg, C.J., Warren, J.M., 2010. Mantle melting, melt transport, and delivery beneath a slow-spreading ridge: the Paleo-MAR from 23°15′N to 23°45′N. Journal of Petrology 51, 425–467.

Ghiorso, M.S., Hirschmann, M.M., Reiners, P.W., Kress, V.C., 2002. The pMELTS: a revision of MELTS for improved calculation of phase relations and major element partitioning related to partial melting of the mantle to 3 GPa. Geochemistry, Geophysics, Geosystems 3.

Green, T.H., Blundy, J.D., Adam, J., Yaxley, G.M., 2000. SIMS determination of trace element partition coefficients between garnet, clinopyroxene and hydrous basaltic liquids at 2–7.5 GPa and 1080–1200 °C. Lithos 53, 165–187.

Grégoire, M., Bell, D.R., Le Roex, A.P., 2003. Garnet lherzolites from the Kaapvaal Craton (South Africa): trace element evidence for a metasomatic history. Journal of Petrology 44, 629–657.

Grégoire, M., Tinguely, C., Bell, D.R., le Roex, A.P., 2005. Spinel lherzolite xenoliths from the Premier kimberlite (Kaapvaal craton, South Africa): nature and evolution of the shallow upper mantle beneath the Bushveld complex. Lithos 84, 185–205.

Griffin, W.L., Graham, S., O'Reilly, S.Y., Pearson, N.J., 2004. Lithosphere evolution beneath the Kaapvaal Craton: Re–Os systematics of sulfides in mantle-derived peridotites. Chemical Geology 208, 89–118.

Handler, M.R., Bennett, V.C., Carlson, R.W., 2005. Nd, Sr and Os isotope systematics in young, fertile spinel peridotite xenoliths from northern Queensland, Australia: a unique view of depleted MORB mantle? Geochimica et Cosmochimica Acta 69, 5747–5763.

Harvey, J., Gannoun, A., Burton, K.W., Rogers, N.W., Alard, O., Parkinson, I.J., 2006. Ancient melt extraction from the oceanic upper mantle revealed by Re–Os isotopes in abyssal peridotites from the Mid-Atlantic ridge. Earth and Planetary Science Letters 244, 606–621.

Heinonen, J.S., Kurz, M.D., 2015. Low-3He/4He sublithospheric mantle source for the most magnesian magmas of the Karoo large igneous province. Earth and Planetary Science Letters 426, 305–315.

Heinonen, J.S., Luttinen, A.V., 2010. Mineral chemical evidence for extremely magnesian subalkaline melts from the Antarctic extension of the Karoo large igneous province. Mineralogy and Petrology 99, 201–217.

Heinonen, J.S., Carlson, R.W., Luttinen, A.V., 2010. Isotopic (Sr, Nd, Pb, and Os) composition of highly magnesian dikes of Vestfjella, western Dronning Maud Land, Antarctica: a key to the origins of the Jurassic Karoo large igneous province? Chemical Geology 277, 227–244.

Hellebrand, E., Snow, J.E., Dick, H.J.B., Hofmann, A.W., 2001. Coupled major and trace elements as indicators of the extent of melting in mid-ocean-ridge peridotites. Nature 410, 677–681.

Herzberg, C., Feigenson, M., Skuba, C., Ohtani, E., 1988. Majorite fractionation recorded in the geochemistry of peridotites from South Africa. Nature 332, 823–826.

Hofmann, A.W., 1988. Chemical differentiation of the Earth: the relationship between mantle, continental crust, and oceanic crust. Earth and Planetary Science Letters 90, 297–314.

Hofmann, A.W., 1997. Mantle geochemistry: the message from oceanic volcanism. Nature 385, 219–229.

Irvine, T.N., 1967. Chromian spinel as a petrogenetic indicator. Part 2. Petrologic applications. Canadian Journal of Earth Sciences 4, 72–103.

Ishikawa, A., Pearson, D.G., Dale, C.W., 2011. Ancient Os isotope signatures from the Ontong Java Plateau lithosphere: tracing lithospheric accretion history. Earth and Planetary Science Letters 301, 159–170.

Johnson, K.T.M., 1998. Experimental determination of partition coefficients for rare earth and high-field-strength elements between clinopyroxene, garnet, and basaltic melt at high pressures. Contributions to Mineralogy and Petrology 133, 60–68.

Johnson, K.T.M., Dick, H.J.B., 1992. Open system melting and temporal and spatial variation of peridotite and basalt at the Atlantis II Fracture Zone. Journal of Geophysical Research: Solid Earth 97, 9219–9241.

Johnson, K.T.M., Dick, H.J.B., Shimizu, N., 1990. Melting in the oceanic upper mantle: an ion microprobe study of diopside in abyssal peridotites. Journal of Geophysical Research 95, 2661–2678.

Jöns, N., Bach, W., Klein, F., 2010. Magmatic influence on reaction paths and element transport during serpentinization. Chemical Geology 274, 196–211.

Kelemen, P.B., Hirth, G., Shimizu, N., Spiegelman, M., Dick, H.J.B., 1997. A review of melt migration processes in the adiabatically upwelling mantle beneath oceanic spreading ridges. Philosophical Transactions of the Royal Society of London Series A 355, 283–318.

Klein, E.M., Langmuir, C.H., 1987. Global correlations of ocean ridge basalt chemistry with axial depth and crustal thickness. Journal of Geophysical Research: Solid Earth 92, 8089–8115.

Kushiro, I., 1969. The system forsterite–diopside–silica with and without water at high pressures. American Journal of Science 267, 269–294.

Kuskov, O.L., Kronrod, V.A., Annersten, H., 2006. Inferring upper-mantle temperatures from seismic and geochemical constraints: implications for Kaapvaal craton. Earth and Planetary Science Letters 244, 133–154.

Lassiter, J.C., Byerly, B.L., Snow, J.E., Hellebrand, E., 2014. Constraints from Os-isotope variations on the origin of Lena Trough abyssal peridotites and implications for the composition and evolution of the depleted upper mantle. Earth and Planetary Science Letters 403, 178–187.

Liu, C.Z., Snow, J.E., Hellebrand, E., Bruegmann, G., von der Handt, A., Buechl, A., Hofmann, A.W., 2008. Ancient, highly heterogeneous mantle beneath Gakkel ridge, Arctic Ocean. Nature 452, 311–316.

Maier, W.D., Peltonen, P., Juvonen, R., Pienaar, C., 2005. Platinum-group elements in peridotite xenoliths and kimberlite from the Premier kimberlite pipe, South Africa. South African Journal of Geology 108, 413–428.

McDonough, W.F., Sun, S.S., 1995. The composition of the Earth. Chemical Geology 120, 223–253.

Niu, Y.L., 1997. Mantle melting and melt extraction processes beneath ocean ridges: evidence from abyssal peridotites. Journal of Petrology 38, 1047–1074.

Niu, Y.L., 2004. Bulk-rock major and trace element compositions of abyssal peridotites: implications for mantle melting, melt extraction and post-melting processes beneath mid-ocean ridges. Journal of Petrology 45, 2423–2458.

Niu, Y.L., Hekinian, R., 1997. Basaltic liquids and harzburgitic residues in the Garrett Transform: A case study at fast-spreading ridges. Earth and Planetary Science Letters v. 146, 243–258.

Niu, Y.L., Regelous, M., Wendt, I.J., Batiza, R., O'Hara, M.J., 2002. Geochemistry of near-EPR seamounts: importance of source vs. process and the origin of enriched mantle component. Earth and Planetary Science Letters 199, 327–345.

Parkinson, I.J., Pearce, J.A., 1998. Peridotites from the Izu–Bonin–Mariana forearc (ODP Leg 125): evidence for mantle melting and melt–mantle interaction in a supra-subduction zone setting. Journal of Petrology 39, 1577–1618.
Pearce, J.A., Barker, P.F., Edwards, S.J., Parkinson, I.J., Leat, P.T., 2000. Geochemistry and tectonic significance of peridotites from the South Sandwich arc–basin system, South Atlantic. Contributions to Mineralogy and Petrology 139, 36–53.
Roy-Barman, M., Allègre, C.J., 1994. $^{187}Os/^{186}Os$ ratios of mid-ocean ridge basalts and abyssal peridotites. Geochimica et Cosmochimica Acta 58, 5043–5054.
Salters, V.J.M., Dick, H.J.B., 2002. Mineralogy of the mid-ocean-ridge basalt source from neodymium isotopic composition of abyssal peridotites. Nature 418, 68–72.
Salters, V.J.M., Longhi, J., 1999. Trace element partitioning during the initial stages of melting beneath mid-ocean ridges. Earth and Planetary Science Letters 166, 15–30.
Salters, V.J.M., Stracke, A., 2004. Composition of the depleted mantle. Geochemistry, Geophysics, Geosystems 5, Q05B07.
Seyler, M., Cannat, M., Mevel, C., 2003. Evidence for major-element heterogeneity in the mantle source of abyssal peridotites from the Southwest Indian Ridge (52° to 68°E). Geochemistry, Geophysics, Geosystems 4.
Simon, N.S.C., Irvine, G.J., Davies, G.R., Pearson, D.G., Carlson, R.W., 2003. The origin of garnet and clinopyroxene in "depleted" Kaapvaal peridotites. Lithos 71, 289–322.
Snow, J.E., Dick, H.J.B., 1995. Pervasive magnesium loss by marine weathering of peridotite. Geochimica et Cosmochimica Acta 59, 4219–4235.
Snow, J.E., Reisberg, L., 1995. Os isotopic systematics of the MORB mantle: results from altered abyssal peridotites. Earth and Planetary Science Letters 133, 411–421.
Snow, J.E., Hart, S.R., Dick, H.J.B., 1994. Nd and Sr isotope evidence linking mid-ocean-ridge basalts and abyssal peridotites. Nature 371, 57–60.
Stracke, A., 2012. Earth's heterogeneous mantle: a product of convection-driven interaction between crust and mantle. Chemical Geology 330–331, 274–299.
Walter, M.J., 1998. Melting of garnet peridotite and the origin of komatiite and depleted lithosphere. Journal of Petrology 39, 29–60.
Weir, N.R.W., White, R.S., Brandsdóttir, B., Einarsson, P., Shimamura, H., Shiobara, H., 2001. Crustal structure of the northern Reykjanes Ridge and Reykjanes Peninsula, southwest Iceland. Journal of Geophysical Research: Solid Earth 106, 6347–6368.
Zeng, Z.G., Wang, Q.Y., Wang, X.M., Chen, S., Yin, X., Li, Z.X., 2012. Geochemistry of abyssal peridotites from the super slow-spreading Southwest Indian Ridge near 65°E: implications for magma source and seawater alteration. Journal of Earth System Science 121, 1317–1336.
Zhao, M.H., Qiu, X.L., Li, J.B.A., Sauter, D., Ruan, A.G., Chen, J., Cannat, M., Singh, S., Zhang, J.Z., Wu, Z.L., Niu, X.W., 2013. Three-dimensional seismic structure of the Dragon Flag oceanic core complex at the ultraslow spreading Southwest Indian Ridge (49°39′ E). Geochemistry, Geophysics, Geosystems 14, 4544–4563.
Zhou, H.Y., Dick, H.J.B., 2013. Thin crust as evidence for depleted mantle supporting the Marion Rise. Nature 494, 195–200.